Journal of Alloys and Compounds 1037 (2025) 182172

Contents lists available at ScienceDirect

Journal of Alloys and Compounds

journal homepage: www.elsevier.com/locate/jalcom

Study on the luminescence mechanism and pressure sensing properties of undoped $Na_8Al_6Si_6O_{24}Cl_2$

Chuchu Song [a], Qingfeng Guo [a,*], Yafang Wang [b], Zheng Deng [c], Changqing Jin [c], Libing Liao [d,*]

[a] School of Gemology, China University of Geosciences, Beijing 100083, China
[b] School of Science, China University of Geosciences, Beijing 100083, China
[c] Institute of Physics, Chinese Academy of Sciences, Beijing, 100190, China
[d] Beijing Key Laboratory of Materials Utilization of Nonmetallic Minerals and Solid Wastes, National Laboratory of Mineral Materials, School of Materials Sciences and Technology, China University of Ge-osciences, Beijing 100083, China

ARTICLE INFO

Keywords:
$Na_8Al_6Si_6O_{24}Cl_2$
Luminescence mechanism
Pressure sensing

ABSTRACT

$Na_8Al_6Si_6O_{24}Cl_2$ is a material with multiple properties such as fluorescence, phosphorescence and photochromism. In this study, the excitation and emission wavelengths of the $Na_8Al_6Si_6O_{24}Cl_2$ matrix were regulated by high temperature solid state reaction under different atmospheres. The luminescence of $Na_8Al_6Si_6O_{24}Cl_2$ under two different excitation bands was achieved, and the intrinsic defect luminescence mechanism model was constructed. Meanwhile, a high-pressure experimental study on $Na_8Al_6Si_6O_{24}Cl_2$ was carried out by combining diamond anvil cell and laser Raman spectroscopy technology. It was found that $Na_8Al_6Si_6O_{24}Cl_2$ synthesized under an Ar atmosphere has good performance in pressure sensing: the Raman shift change under high pressure can reach 5.87 cm^{-1}/Gpa. This work not only discovered a low-cost intrinsic defect luminescent material free of rare earths and expensive metal ions, but also for the first time found the application prospects of $Na_8Al_6Si_6O_{24}Cl_2$ material in pressure.

1. Introduction

Compared with traditional luminescent matrix materials, framework silicate have developed into an important matrix of photoluminescent materials and cathode ray luminescent materials due to their good chemical and thermal stability and the inexpensive and easy availability of high-purity silica raw materials [1,2]. Sodalite is a typical silicate mineral with a shelf-like structure, and its crystal structure consists of cuboctahedral cages of AlO_4 and SiO_4. These cages are surrounded by five six-membered tetrahedral rings and six four-membered rings, which have strong stability [3–5] Meanwhile, as a good luminescent material, sodalite has been reported for fluorescence and phosphorescence studies in recent years.

Most of the current studies have modulated the luminescence properties of sodalite by doping rare earth ions, transition metal ions, such as doping Eu^{3+}, Tb^{3+}, Ce^{3+}, Ti^{3+}, etc. Eu^{3+} often acts as a red fluorescence center in sodalite matrix [6,7], and sensitization of Eu^{3+} by Bi^{3+} greatly enhances the luminescence intensity [8]. The Tb^{3+} ion jump emission is about 550 nm, and the emission spectrum under 242 nm excitation produces a series of narrow-band peaks due to the Tb^{3+} ion $^5D_3 \rightarrow {}^7F_J$ and $^5D_4 \rightarrow {}^7F_5$ [9]. And the co-doping of Ce^{3+} and Tb^{3+} not only enhances the luminescence intensity of Tb^{3+} under long-wave UV light, but also enriches its excitation wavelength [10,11]. And the special variety of sodalite, $Na_8Al_6Si_6O_{24}(Cl,S)_2$, was made into $(Li,Na)_8Al_6Si_6O_{24}(Cl,S)_2$:2 % Ti material by doping Li and Ti, which has long afterglow properties [12,13]. But the luminescence of the sodalite matrix itself has been less studied.

$Na_8Al_6Si_6O_{24}Cl_2$ is one of the most basic varieties of sodalite, with a crystal structure featuring a microporous structure with a cross-channel system and a highly elastic framework. It has a wide range of thermodynamic stability conditions and has applications in ion exchange, immobilization, ionic conductivity and luminescence [14,15]. $Na_8Al_6Si_6O_{24}Cl_2$ can be used as a matrix for luminescent materials as well as an intrinsic defective luminescent material that can be luminescent without doping ions. Existing studies have found that $Na_8Al_6Si_6O_{24}Cl_2$ has an emission peak around 450 nm and can continue to emit light even after the excitation light source is stopped [16]. Some studies have suggested that the luminescence of the substrate is related to O_2^- [17], while others have suggested that the luminescence is related to oxygen vacancies [17] or S [18], but it still has not been systematically confirmed.

* Corresponding authors.
E-mail addresses: qfguo@cugb.edu.cn (Q. Guo), clayl@cugb.edu.cn (L. Liao).

https://doi.org/10.1016/j.jallcom.2025.182172
Received 12 June 2025; Received in revised form 4 July 2025; Accepted 8 July 2025
Available online 11 July 2025

Currently, such as fluorine oxides $Sr_{3-x}A_xMO_4F$ (A=Ca / Ba; MGa / A1) [19,20], fluorosilicates $La_3F_3(Si_3O_9)$ [21], phosphates BPO_4 [22], as well as $CdSiO_3$ [23], and $CaSb_2O_6$ [24], etc., are known as intrinsic defect luminescent materials. Compared to these materials, $Na_8Al_6Si_6O_{24}Cl_2$ is more economical as the raw materials are more readily available and cheap, and the synthesis and processing costs are lower. Given these economic advantages along with its unique luminescent properties, $Na_8Al_6Si_6O_{24}Cl_2$ holds great potential for practical applications in optoelectronic devices and energy-saving technologies. Therefore, it is of practical significance to study the luminescence properties and luminescence mechanism of $Na_8Al_6Si_6O_{24}Cl_2$.

In this paper, $Na_8Al_6Si_6O_{24}Cl_2$ was synthesized under different atmospheres, and its luminescence properties were regulated. The samples were characterized by X-ray diffraction, fluorescence spectroscopy, electron paramagnetic resonance spectroscopy, thermoluminescence spectroscopy, positron annihilation lifetime spectroscopy, etc., to comprehensively explore the luminescence characteristics and luminescence mechanism of $Na_8Al_6Si_6O_{24}Cl_2$ under different synthesis conditions. Meanwhile, the study combined diamond anvil cell (DAC) and laser Raman spectroscopy technology. High-pressure experimental research was carried out on $Na_8Al_6Si_6O_{24}Cl_2$ synthesized under the conditions of 8 % H_2 + 92 %N_2 and Ar atmosphere. It was found that the Raman shift of $Na_8Al_6Si_6O_{24}Cl_2$ synthesized under the Ar atmosphere showed a relatively perfect linear relationship with the pressure change. It has broad prospects in the application of pressure sensing.

2. Materials and methods

2.1. Materials

Samples N-1, N-2, N-3, and N-4 were $Na_8Al_6Si_6O_{24}Cl_2$ that synthesized under different conditions.

Sample N-1 was synthesized by solid phase method. Dry zeolite A (0.744 g, Sigma-Aldrich, product no. 96096), NaCl (0.117 g, J.T. Barker, 99.5 %) powder was mixed. H_3BO_3 with a mass of 0.682 g was added as a flux. The mixture was heated in air at 850 °C for 20 h and the temperature increase rate of 5 °C/s. After the product was freely cooled to room temperature, it was heated at 850 °C for an additional 2 h under a flowing atmosphere of 8 % H_2 + 92 % N_2 and then cooled again to room temperature. A final wash with water was performed to remove excess NaCl impurities.

Sample N-2 was synthesized by solid phase method. Zeolite A (0.744 g, Sigma-Aldrich, product no. 96096), NaCl (0.117 g, J.T. Barker, 99.5 %) powder was mixed. H_3BO_3 with a mass of 0.682 g was added as a flux. The mixture was heated in air at 850 °C for 20 h (The temperature increase rate of 5/s) and then cooled to room temperature. It was finally washed with water to remove excess NaCl impurities.

Sample N-3 was synthesized by solid phase method. Zeolite A (0.744 g, Sigma-Aldrich, product no. 96096), NaCl (0.117 g, J.T. Barker, 99.5 %) powder was mixed. H_3BO_3 with a mass of 0.682 g was added as a flux. The double crucible method was used, where the mixture was placed in a small internal crucible and the inside of the large crucible was filled with C. The mixture was placed in air at 850 °C for 20 h (The temperature increase rate of 5° C/s) and then cooled to room temperature. A final wash with water was performed to remove excess NaCl impurities.

Sample N-4 was synthesized by solid phase method. A-type zeolite (0.744 g, Sigma-Aldrich, product no. 96096), NaCl (0.117 g, J.T. Barker, 99.5 %) powder was mixed. H_3BO_3 with a mass of 0.682 g was added as a flux. The mixture was heated in Ar gas at 850 °C for 20 h (The temperature increase rate of 5 °C/s) and then cooled to room temperature. It was finally washed with water to remove excess NaCl impurities.

2.2. Method

X-ray diffraction experiments were carried out using a D8Advance X-ray diffractometer manufactured by Bruker AXS GmbH, Germany, with a resolution of 0.0001 mm, a focal spot size of 0.4 × 12 mm, a maximum output power of 3 kW, a copper target, Kα-rays, and a scanning speed of 0.17 °/s. The Rietveld refinement analysis was carried out using the GSAS II. We mainly utilized the refinement module of GSAS II. By adjusting the parameters of the crystal structure model, we made the calculated diffraction patterns best fit the experimental diffraction patterns. During the refinement process, we focused on key parameters such as cell parameters, atomic positions, occupancy degrees, and anisotropic temperature factors to ensure the accuracy and reliability of the refinement results. Fluorescence spectra of the samples were measured using a Hitachi F-4700 instrument for the fluorescence and emission spectra and excitation spectra. emission spectrum and excitation spectrum. Three-dimensional pyroelectric spectroscopy was performed using a TOSL-3DS pyroelectric photoluminescence three-dimensional spectrometer from Guangzhou Ruidi Aisheng Technology Co., Ltd. in China, with a temperature range of 300–450 K and a temperature increase rate of 3° C/s, the amount of powder is 0.16 g. Electron paramagnetic resonance (EPR) spectroscopy was performed using an ESR5000 electron paramagnetic resonance spectrometer from Bruker, Germany, with a testing temperature of 90 K. The positron annihilation lifetime test was conducted using the AMETEK PLS-SYSTEM positron annihilation lifetime spectrometer. The size of the sample thin film lamination was 1*1 mm and 3.5*3.5 mm. The symmetric DAC is adopted. The diameter of the diamond anvil surface is 300 μm, the gasket is rhenium sheet with a thickness of 0.25 mm, and a small hole with a diameter of approximately 200 μm is machined in the center as the sample chamber. Ruby is used to measure pressures. The powdered samples of the experiment were directly placed in the diamond anvil cell under the microscope. And the sample should be placed in the central hole of the sealing gasket, ensuring that the sample is at the focal point of the diamond pressure head. By adjusting the pressure screw of the diamond opposed anvil press, the diamond presses the pressure chamber, thereby increasing the pressure within the pressure chamber. The Raman spectroscopy test was conducted using the HR-Evolution micro-Raman spectrometer, with the excitation light source being 532 nm.

3. Results and discussion

3.1. Structural analysis

X-ray diffraction patterns often reflect the structural information of materials. Experiments were done to analyze the X-ray diffraction of N-1, N-2, N-3, and N-4 samples, respectively, and the Rietveld refinements (The model used is $Na_8Al_6Si_6O_{24}Cl_2$ an d COD ID is 1011185) were resulted using GSAS II. As shown in Fig. 1, $Na_8Al_6Si_6O_{24}Cl_2$ has a special $(Na_4Cl)^{3+}$ cage structure consisting of AlO_4 and SiO_4 tetrahedral rings, and its aluminosilicate framework has a cubic symmetry and consists of successive alternating layers containing six-membered rings of silicon and aluminum-centered tetrahedra alternating around the triple axes

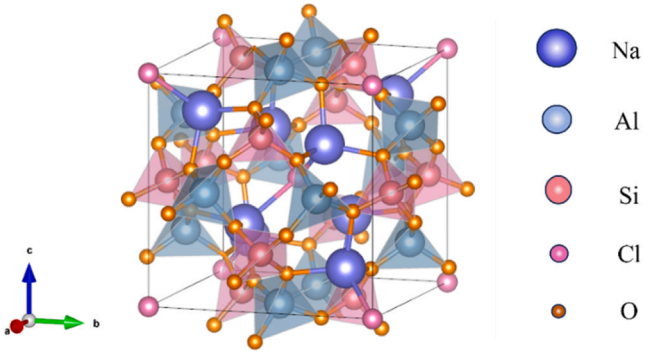

Fig. 1. The structure of $Na_8Al_6Si_6O_{24}Cl_2$.

[1/32/3z], [2/3/3z] and [0 0 z]. Based on the results Table S1 and the diffraction patterns of Fig. 2, it is known that all four samples of galena synthesized under different atmospheres are pure phases and belong to the space group P43n (No. 218).

The cell parameters of the samples were further analyzed and calculated as shown in Table. S1, and the average cell parameters of the samples were a = b = c = 0.88728 nm, α = β = γ = 90°, and V = 0.69852 nm^3, which were similar to those of the standard calcite, and the cell parameters of N-1 were slightly larger than those of N-2 and N-3. Based on the results in Table 1, it can be seen that the O occupancy degree of the samples was less than 1 in the samples, 5.0 % in N-1, 5.3 % in N-2, and oxygen vacancies in N-3. O occupancy in the samples are all less than 1, and oxygen vacancies exist in the samples. The oxygen vacancy rate of N-1 is 5.0 %, N-2 is 5.3 %, N-3 is 3.3 %, and N-4 is 5.5 %. The remaining structural information can be found in Table. S2.

3.2. Component analysis

We used X-ray fluorescence spectrometry (XRF) for component analysis, and the results are shown in Table 2. The main element composition of All samples is Na, Al, Si, Cl and O. In addition, there are metallic elements (Ca, K, Ag, Zr), transition metal elements (Fe, Ni, Cu, Cr, Ti, Zn), non-metallic elements (S), rare earth elements (Nb, Ir, Bi, etc.). The average Na_2O content of N-1, N-2, N-3, N-4 is 41.294 % he

Table 1
Occupancy of each atom obtained by Rietveld refinement.

Sample	frac Na	frac Al	frac Si	frac O	frac Cl
N−1	1.102	1.01	1.018	0.950	1.056
N−2	1.099	1.01	1.025	0.947	1.007
N−3	1.073	0.999	1.010	0.967	1.033
N−4	1.158	1.055	1.013	0.945	1.072

average Al_2O_3 content is 26.634 %, the average content of SiO_2 is 26.458 % and the average content of Cl is 4.991 %.

3.3. Luminescence properties

In order to investigate the luminescence properties of the samples, we performed fluorescence spectroscopy tests on all four samples. As shown in the results of Fig. 3a b, the excitation wavelength of the N-1 sample synthesized under 8 % H_2 + 92 % N_2 was in at around 205 nm and the emission wavelength was at around 434 nm. While the excitation and emission wavelengths of N-2, N-3, and N-4 samples were shifted, with the strongest excitation wavelength at around 278 nm and emission wavelength at around 500 nm. The intensities of the emission spectra were N-4, N-1, N-3, and N-2 in descending order.

Figure. S1a shows the color coordinate plot of the N-1 sample with

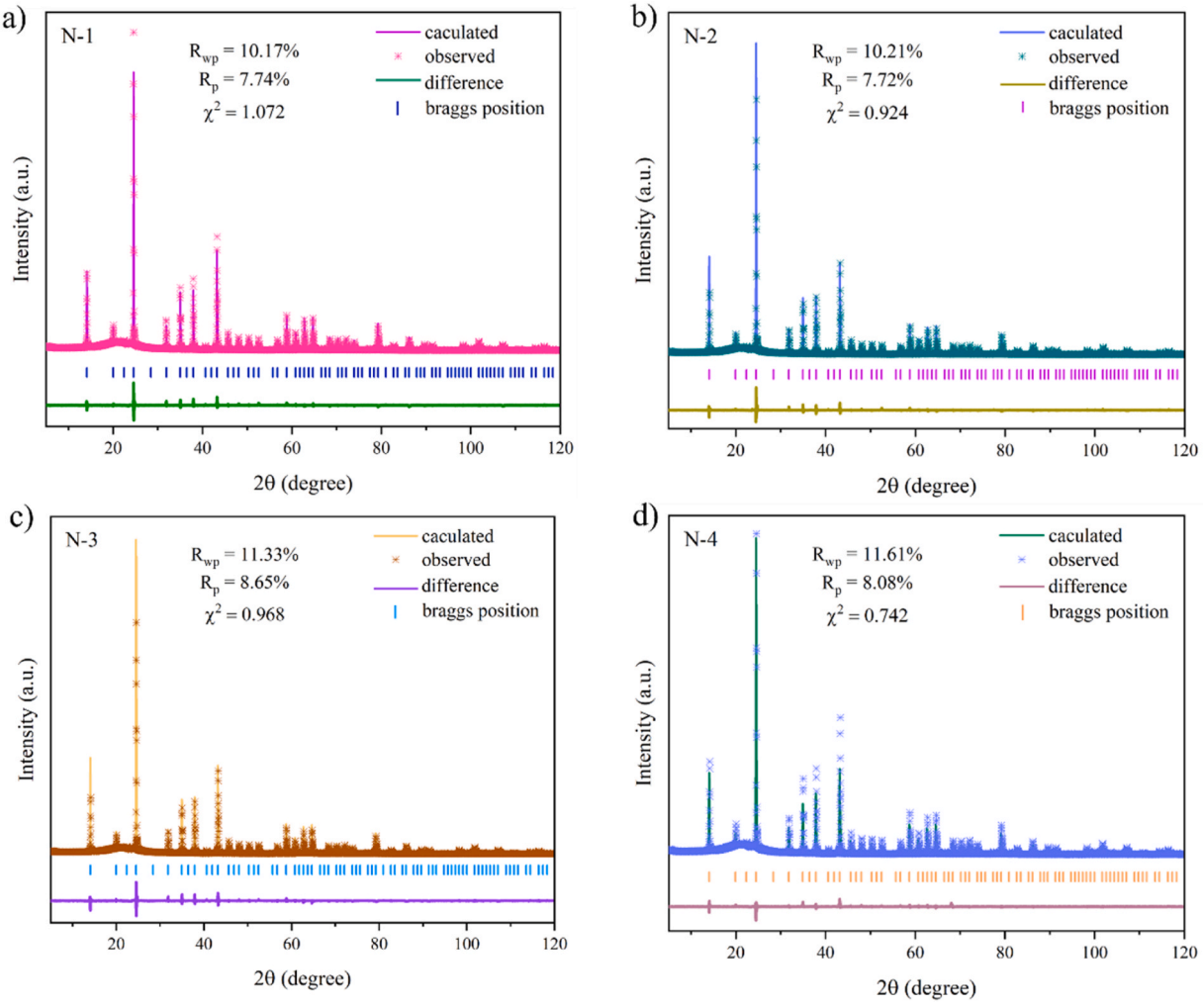

Fig. 2. Rietveld plots for the studied sample. R_{wp} (Weighted Profile R-factor): this is the weighted profile R-factor, which is used to assess the difference between the calculated and experimental spectral lines. R_p (Profile R-factor): this is the profile R-factor, which is used to assess the consistency of the refinement results with the experimental data. χ2: This is the chi-square value, which measures the degree of conformity between the refined model and the experimental data. a) Rietveld plots for N-1; b) Rietveld plots for N-2; c) Rietveld plots for N-3; d) Rietveld plots for N-4.

Table 2
X-ray Fluorescence spectra analysis data of samples (wt%).

Sample	N-1	N-2	N-3	N-4
Na_2O	41.315	42.230	41.233	40.399
Al_2O_3	26.738	26.276	26.671	26.851
SiO_2	26.373	26.013	26.501	26.943
Cl	5.019	4.838	4.991	5.115
SO_3	0.423	0.520	0.474	0.568
CaO	0.042	0.040	0.049	0.043
K_2O	0.032	0.031	0.042	0.039
Fe_2O_3	0.017	0.013	0.011	0.014
TiO_2	0.009	0.012	0.008	0.009
CuO	0.007	0.009	0.007	0.007
Ag_2O	0.001	0.006	0.000	0.000
V_2O_5	0.006	0.005	0.007	0.000
Ir_2O_3	0.004	0.003	0.000	0.003
ZrO_2	0.002	0.002	0.002	0.002
ZnO	0.000	0.002	0.000	0.002
$Bi2O_3$	0.007	0.000	0.000	0.005
Cr_2O_3	0.004	0.000	0.000	0.000
NbO	0.000	0.001	0.000	0.000
NiO	0.000	0.000	0.003	0.000
GeO_2	0.000	0.000	0.000	0.002
Total	99.999	100.001	99.999	100.002

(0.182, 0.159) and 68.68 % color purity under the excitation of 215 nm light source; Figure. S1b shows the color coordinate plot of the N-2 sample with (0.211, 0.382) and 38.64 % color purity under the excitation of 270 nm light source; the Figure. S1c shows the color coordinate diagram of N-3 sample with the color coordinate of (0.215, 0.371) and the color purity of 37.80 % under the excitation of 270 nm light source; Figure. S1d shows the color coordinate diagram of N-4 sample with the color coordinate of (0.201, 0.368) and the color purity of 37.81 % under the excitation of 270 nm light source. The color purity of the four samples is the highest in N-1, while the color purity of N-2, N-3, and N-4 is basically comparable.

According to NTSC (National Television Systems Committee), the standard blue color coordinate is (0.14, 0.08), the standard green color coordinate is (0.21, 0.71) and the standard red color coordinate is (0.67, 0.33). Upon comparative analysis, the fluorescence emitted by the sample N-1 synthesized under 8 % H_2 + 92 % N_2 is closer to blue light, while the sample N-2 synthesized under air condition, the sample N-3 synthesized by the double crucible method, and the sample N-4 synthesized under the Ar gas atmosphere are significantly shifted to green light. It indicates that different synthesis conditions can change the luminescence properties of $Na_8Al_6Si_6O_{24}Cl_2$.

And in Figure. S2 a, b, we can find that the phosphorescence lifetimes of the four samples can be measured, and the phosphorescence lifetime of N-1 is longer, with an average lifetime of 1.776 s, while the phosphorescence lifetimes of N-2, N-3, and N-4 are significantly shorter.

3.4. Thermoluminescence properties

In order to further investigate the effect of defects on the luminescent properties of the samples, the experimental N-1, N-2, N-3, and N-4 samples were subjected to thermoluminescence spectroscopy.

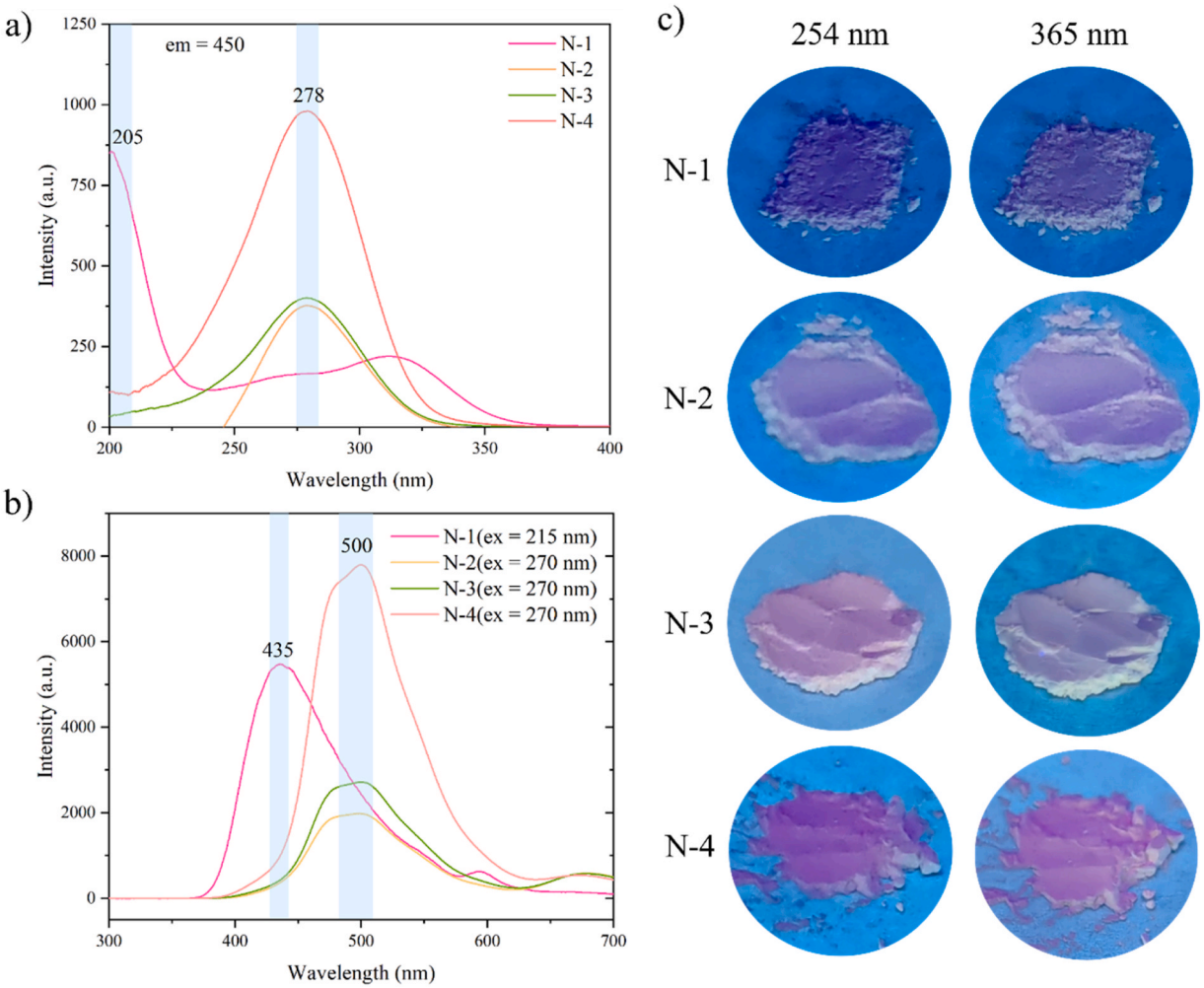

Fig. 3. a) Excitation spectra of the samples; b) Emission spectra of the samples; c) Luminescence of the samples under 365 and 254 nm irradiation.

The experimental results (Fig. 4) showed that the intensity of the thermoluminescence glow curve of sample N-1 was significantly stronger than that of samples N-2, N-3, and N-4 after irradiation for 5 min under 254 nm and 365 nm UV light. The distance between the UV source and the samples is 20 cm. The luminescence peaks of N-1 were more symmetric, and the intensity of the thermoluminescence. curve was significantly stronger after irradiation with 254 nm UV light than that after irradiation with 365 nm UV light. The peaks of samples N-2, N-3, and N-4 are obviously asymmetric and are the superposition of several peaks, while the intensity of the thermoluminescence curves of samples N-2, N-3, and N-4 is the opposite of that of sample N-1, and is significantly stronger under 365 nm irradiation than under 254 nm irradiation. This result indicates that the defect type of sample N-1 is different from that of N-2, N-3, and N-4, and its luminescence mechanism is also different. In order to further investigate the defects in the samples, in this paper, the curves of the pyroelectricity of N-1 and -N-4 have been calculated using the Computerized glow curve inverse fold product (CGCD) method. Glow curve fitting and the traps depth of TL peaks are also calculated by computerized glow curve deconvolution (CGCD) techniques. The TL reader we used is Tangdate. After the experiment imported the TL data into the TL reader, the temperature was first fitted. Then select the TL general kinetic fitting function, add the peaks to the appropriate location, and click Fit Current Curve, the TL reader will fit the curve according to the selected function and display the relevant parameters.

The results of the curve fitting are shown in Fig. 4e, f. The CGCD method is a very important method for calculating the kinetic order of the pyroelectricity of crystals, as well as the trap energy levels [22,25]. This method usually uses the Kitis equation: [26]

$$\mathbf{I(t)} = \boldsymbol{I_m b^{\frac{b}{b-1}}} \exp\left(\frac{\boldsymbol{E}}{\boldsymbol{kT}}\frac{\boldsymbol{T-T_m}}{\boldsymbol{T_m}}\right) \times [(\boldsymbol{b-1})(\boldsymbol{1-\Delta})\frac{\boldsymbol{T^2}}{\boldsymbol{T_m^2}}\exp\left(\frac{\boldsymbol{E}}{\boldsymbol{kT}}\frac{\boldsymbol{T-T_m}}{\boldsymbol{T_m}}\right) + \boldsymbol{Z_m}]^{-\frac{b}{b-1}}$$

$\Delta = 2kT/E$, $\Delta_m = 2kT/E$, $Z_m = 1 + (b\text{-}1)\,\Delta_m$, I is the strength of the TL, E is the activation energy (in eV), Im is the maximum peak strength, b is the order of the kinetics, k is the Boltzmann constant, T is the thermodynamic temperature (in K), and Tm is the maximum peak thermodynamic temperature.

As can be seen from Fig. 4e, f, the thermoluminescence profile of N-1 after 254 nm irradiation 1 peak at 350 K, and the trap depth is about 1.556 eV according to the algorithm, and the thermoluminescence profile of N-4 after 365 nm irradiation can be fitted as 2 peaks at 350 K and 415 K, with trap depths of 1.550 and 1.561 eV, respectively. The rest of the related parameters can be seen in Table. S3. A review of the literature reveals that the single peak obtained from the fit of N-1 at 350 K is related to oxygen vacancies, while the double peak of N-4 may be a composite vacancy pair consisting of oxygen vacancies and other vacancies [27].

3.5. Electron paramagnetic resonance spectroscopy

As shown in Fig. 5a, we can see that the signal of g = 2.009 is significantly weakened after the N-1 sample was irradiated with 254 nm UV light for 5 min at 90 K. After reviewing the literature, it was found that there are two signals of g = 2.009 and g = 2.007 oxygen vacancies in sodalite [12,13]. In our experiments, we did not observe the signal for g = 2.007, which may be related to the difference between the test temperature and the dopant ions. In contrast, the weakened signal for g = 2.009 represents that some carriers are trapped by oxygen vacancies after UV irradiation, leading to a decrease in the concentration of oxygen vacancies and a weakened signal. This result further verifies that the presence of oxygen vacancies in the N-1 sample and their ability to trap carriers are responsible for the luminescence. At the same time, we found that the change of this signal is almost unobservable under room temperature conditions (Figure. S3). After irradiation at 254 nm for 5 min, the intensity was essentially unchanged when tested at room temperature. It may be due to the fact that room temperature conditions cause the trapped carriers to quickly get out of the oxygen vacancy trap,

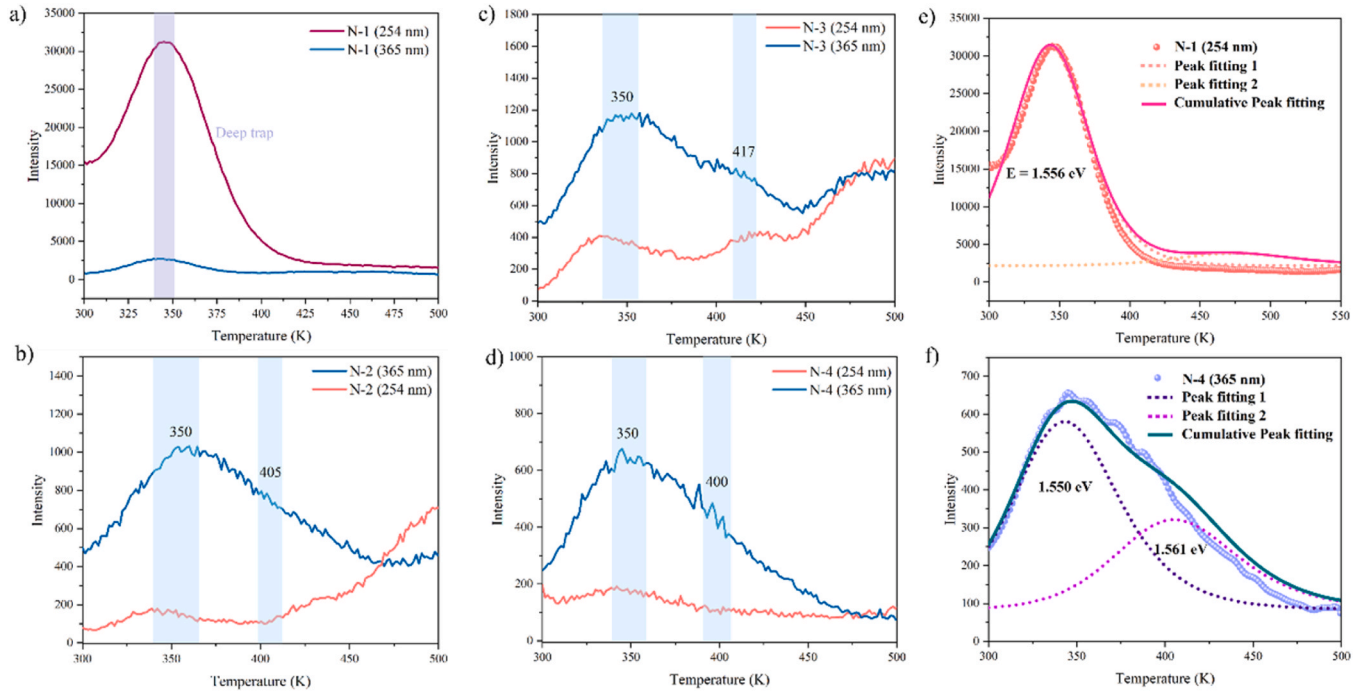

Fig. 4. a) Thermoluminescence curve of sample N-1 under UV irradiation at 254 nm vs. 365 nm; b) Thermoluminescence curve of sample N-2 under UV irradiation at 254 nm vs. 365 nm; c) Thermoluminescence curve of sample N-3 under UV irradiation at 254 nm vs. 365 nm; d) Thermoluminescence curve of sample N-4 under UV irradiation at 254 nm vs. 365 nm. e) Thermoluminescent decomposition curve of sample N-1 under 254 nm UV irradiation f) Thermoluminescent decomposition curve of sample N-4 under 365 nm UV irradiation.

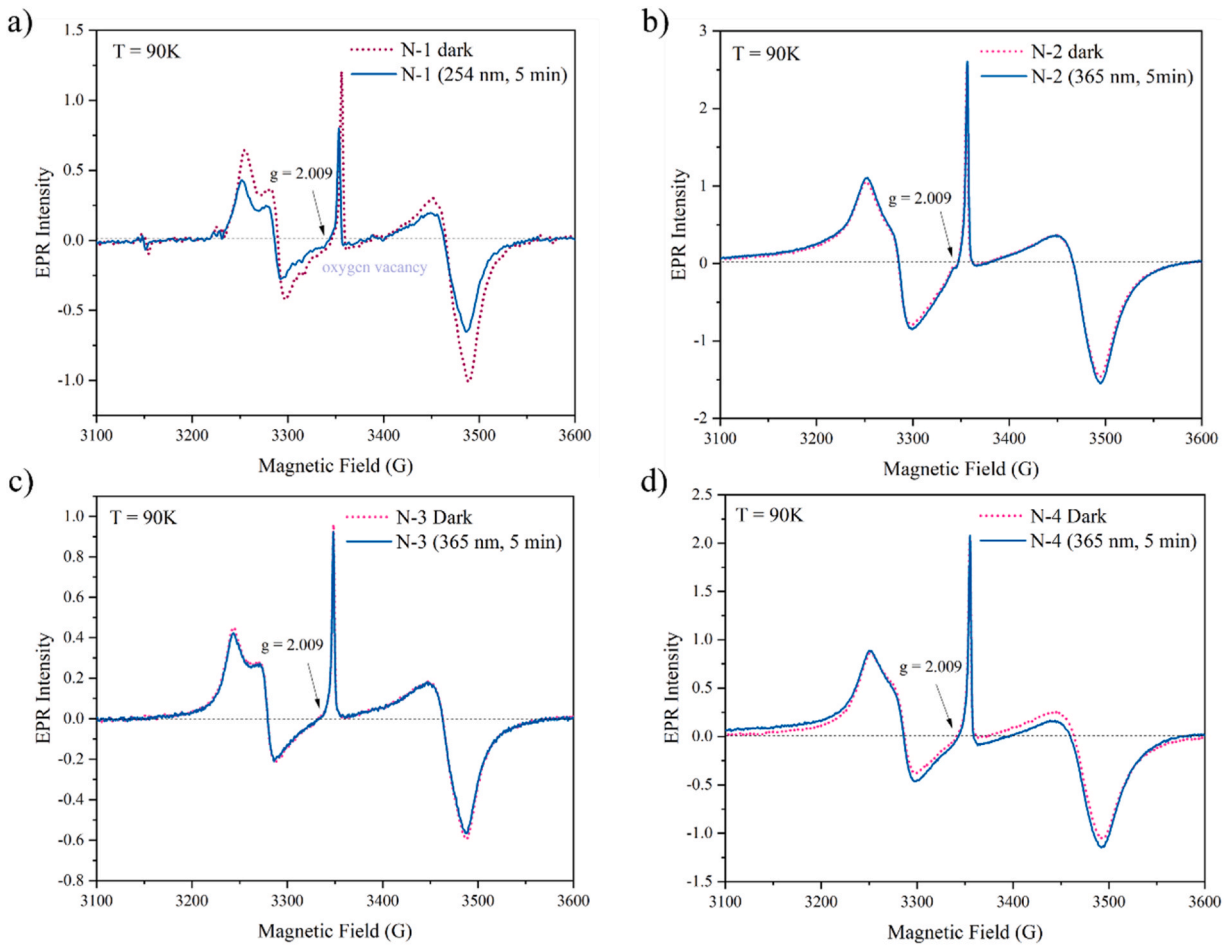

Fig. 5. a) Electron paramagnetic resonance spectrum of N-1 at 90 K; b) Electron paramagnetic resonance spectrum of N-2 at 90 K; c) Electron paramagnetic resonance spectrum of N-3 at 90 K; d) Electron paramagnetic resonance spectrum of N-4 at 90 K.

which makes it difficult to observe.

In Fig. 5a, b, c, we can observe that the signals at g = 2.009 are essentially unchanged after irradiation in N-2, N-3, and N-4. This suggests that the luminescence mechanism of N-1 is different from that of N-2, N-3, N-4. N-1 may be associated with oxygen vacancies, while the luminescence of the other three samples is influenced by other vacancies.

3.6. Positron annihilation lifetime

The positron annihilation lifetime is one of the most effective tools for obtaining information on the internal microstructure and micro-defects in condensed matter, and it is highly sensitive to atomic-scale structural defects (such as single vacancies, double vacancies and vacancy clusters and various color centers) in various crystalline materials [28]. In this paper, positron annihilation lifetime spectra were measured for samples N-1 and N-4. The test results are shown in Figure. S4 and Table 3 presents the positron lifetimes Lifetime1, Lifetime2, Lifetime3 and relative intensities Intensity1, Intensity2, Intensity3 of samples N-1 and N-4. The lifetime spectra were fitted with three lifetime components using the LifeTime(V9) program. Lifetime1 represents the free annihilation of positrons and the annihilation in the single-vacancy capture state; Lifetime2 represents the annihilation lifetime of positrons captured by vacancy clusters [28,29]; Lifetime3 represents the annihilation lifetime of positrons forming positron bound states in the samples, which is caused by the positron-ion pairs formed in the air-filled spaces between powders and is not related to microstructural defect [30,31]. We do not discuss this.

The positron annihilation lifetime under different defects was calculated by using the two-component density functional theory (TCDFT) [32,33]. The charge density is read as AECCAR0 (core electron density) and AECCAR2 or CHGCAR (valence electron density). The model is iteratively calculated through VASP [34,35]. The results are in Table 4. And the positron wave function distribution at different defects in $Na_8Al_6Si_6O_{24}Cl_2$ is in Fig. 6.

From this, we can infer that oxygen vacancies have an impact on the luminescence of N-1. Combination with the results in Fig. 4a, it is known that the defect affecting the luminescence of the N-1 sample is a single vacancy, so we do not consider the influence of the vacancy pair represented by Lifetime2 on N-1. The detailed calculations is shown in Positron annihilation lifetime calculations and Positron annihilation lifetime calculation process (supporting information). According to

Table 3
Positron annihilation lifetime (ps) solution spectra measured for N-1 and N-4.

Sample	Lifetime1	Intensity1	Lifetime2	Intensity2	Lifetime3	Intensity3
N−1	127	20.58	366	37.19	886	42.24
N−4	215	37.56	573	36.36	1032	26.08

Table 4
Positron annihilation lifetimes calculated using TCDFT.

Defect	Positron Annihilation Lifetime
V_{Na}	209.5 ps
V_{Al}	212.8 ps
V_{Si}	168.3 ps
V_O	133.7 ps
V_{Cl}	124.6 ps
V_{Na}-V_{Na}	266.8 ps
V_{Al}-V_{Al}	263.2 ps
V_{Si}-V_{Si}	204.3 ps
V_O-V_O	239.5 ps
V_{Cl}-V_{Cl}	175.6 ps
V_O-V_{Al}	566.9 ps
V_O-V_{Si}	495.4 ps
V_O-V_{Na}	523.1 ps

Table 3 and Table 4, the lifetime 1 of N-1 is 127 ps, which is similar to the positron annihilation lifetimes of V_O (133.7 ps) and V_{Cl} (124.6 ps). However, the trap depth of V_{Cl} in $Na_8Al_6Si_6O_{24}Cl_2$ is generally 1.3 eV [27], which is not consistent with the trap depth of 1.556 eV calculated in Fig. 5. And the actual and theoretical values of trap depth and positron annihilation lifetime of V_O are able to correspond to each other and are within the error range. Therefore, we consider the luminescence defect of N-1 as V_O. For the N-4 sample, Lifetime1 is 215 ps and Lifetime2 is 573 ps, significantly higher than the 127 ps and 0.366 ns of N-1. This is because the Lifetime1 of the sample includes the bulk lifetime and the positron lifetime in single vacancy defects, such as Si vacancies and Al vacancies. The Al: Si ratio of the N-1 sample is 0.524:0.439 = 1.19, and that of the N-4 sample is 0.526:0.448 = 1.17. It can be seen that the proportion of Al in N-4 has decreased. Therefore, it is deduced that Lifetime1 includes the positron annihilation lifetime of Al vacancies, while Lifetime2 represents the V_O-V_{Al} vacancy pair. Similarly, in combination with the results in Fig. 4b, we believe that the defect affecting the luminescence of the N-4 sample is the vacancy pair, namely the V_O-V_{Al} vacancy pair. According to the results in Table 3 and Table 4, the lifetime 2 of N-4 corresponds to the theoretical lifetime 566.9 ps of V_O-V_{Al} Progress verifies the results.

3.7. Luminescence mechanism

Research shows that the presence of defects in intrinsic defect luminescent materials can perturb the local potential field within the material's band gap, introducing additional defect levels. When electrons and holes are trapped by these defect levels, some localized levels are generated between the band gap, with deep levels mainly functioning as traps or recombination centers [36,37]. Electrons and holes will transition between the localized levels and the conduction band minimum, thereby recombining and emitting photons. This process is called defect luminescence and is characterized by broad-band emission [36]. Meanwhile, oxygen vacancies in $Na_8Al_6Si_6O_{24}Cl_2$ materials act as hole traps, located below the Fermi level [27]. Based on the above data, we can construct a schematic diagram of the luminescence mechanism for N-1 and N-4, as shown in Fig. 7. The excitation energy is around 6.04 eV (205 nm) and 4.48 eV (278 nm), where holes in the matrix are excited (process 1); holes move from these excited levels to the valence band and are captured by defects (process 2) V_O or V_O-V_{Al} (process 3); thermal energy prompts holes to transfer from traps to the valence band (process 3); holes relax and emit a broad peak at 2.5 eV (500 nm) (process 4).

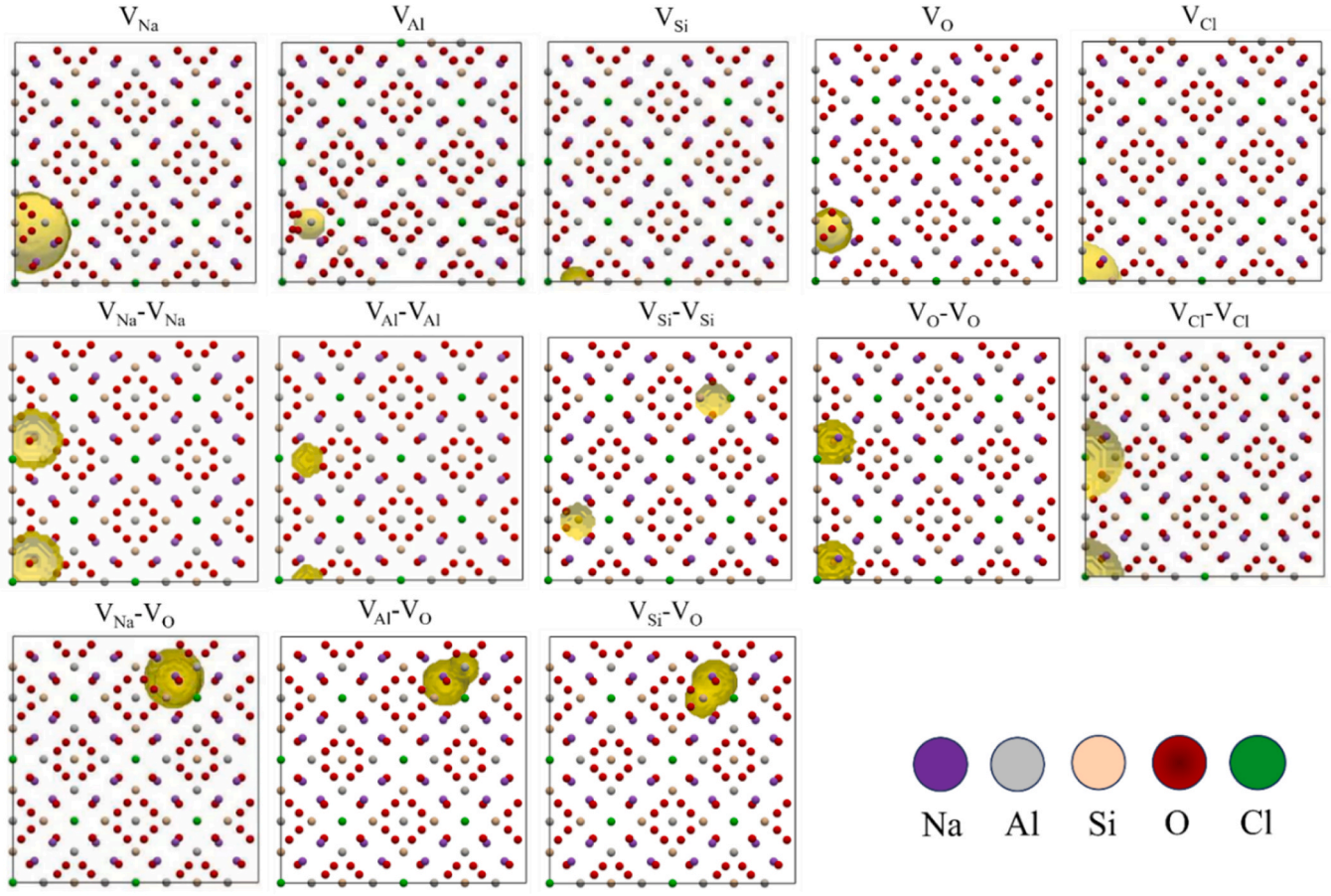

Fig. 6. Positron wave function distribution (yellow area) at different defects in $Na_8Al_6Si_6O_{24}Cl_2$.

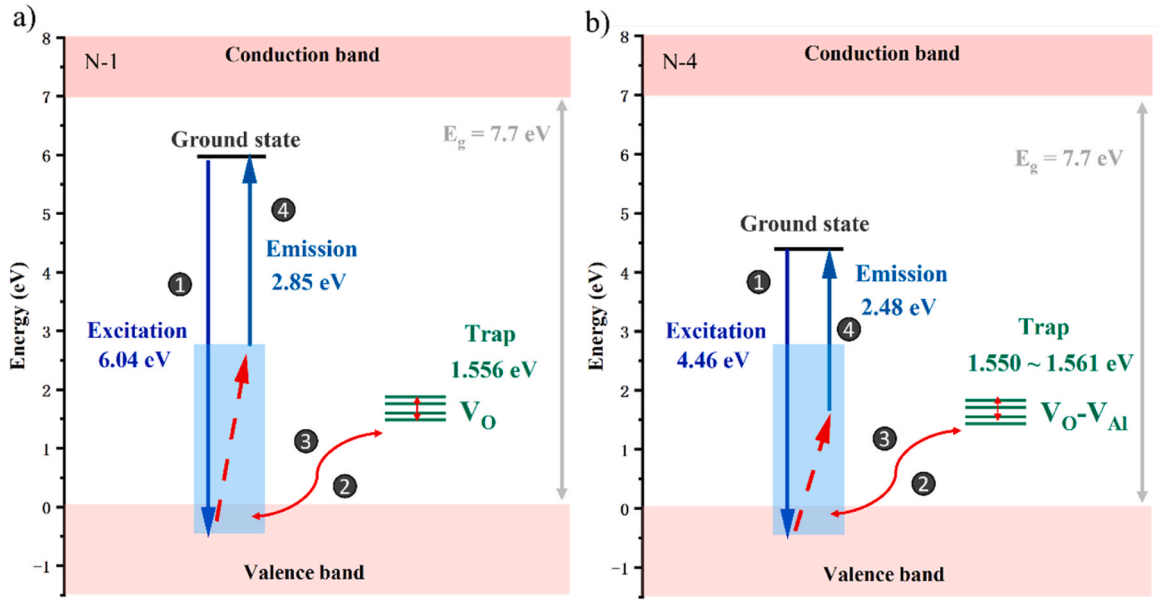

Fig. 7. Diagrams of the luminescence mechanisms of the samples. a) Diagram of the luminescence mechanism of sample N-1; b) Diagram of the luminescence mechanism of sample N-4.

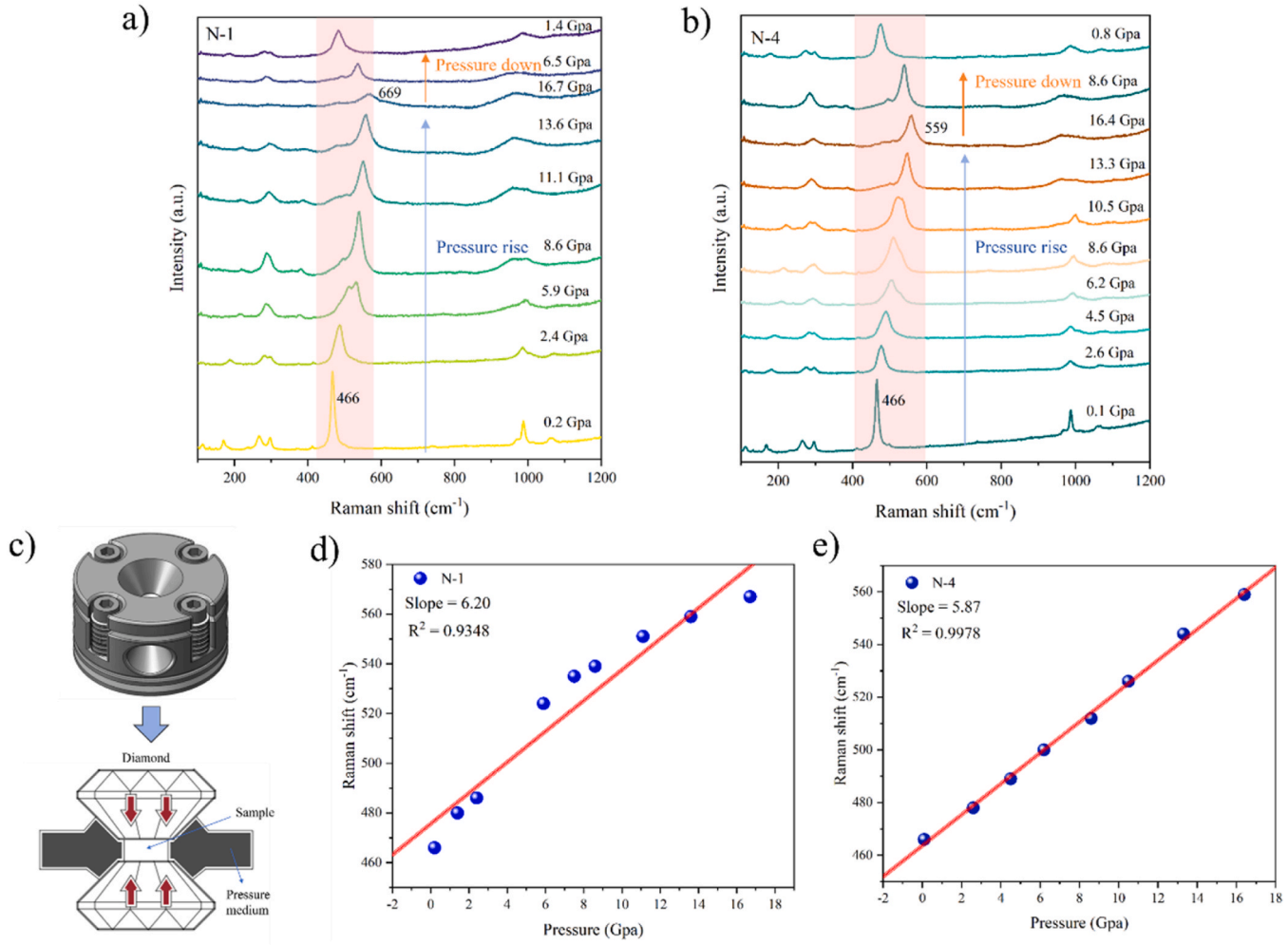

Fig. 8. a) Raman spectra of N-1 sample under different pressures; b) Raman spectra of N-4 sample under different pressures; c) Schematic diagram of the diamond pressure chamber principle; d) Linear fitting diagram of Raman shift of N-1 under different pressures; e) Linear fitting diagram of Raman shift of N-4 under different pressures.

3.8. Pressure-variable Raman spectroscopy

Fig. 8 shows the trend of Raman peaks of $Na_8Al_6Si_6O_{24}Cl_2$ with pressure variation. The peak at 466 cm^{-1} is caused by the stretching of the $ClNa_4$ tetrahedron, the bending of Si-O, the vibration of SiO_4, or the v mode of T-O-T [38–40]. As shown in Fig. 8a, the Raman peak at 466 cm^{-1} of N-1 sample shifts redward with the increase of the system pressure. When the pressure is increased to 5.9 GPa, the Raman peak splits, indicating that the system undergoes a phase transition. Further increasing the pressure causes the characteristic peak to broaden and shift to a higher frequency. When the system pressure reaches 16.7 GPa, the characteristic peak has broadened and almost disappeared. When the system is depressurized, the characteristic peak shifts blueward and gradually returns to its original state, proving that the phase transition of N-1 under high pressure is an reversible phase transition. As shown in Fig. 8b, the Raman peak at 466 cm^{-1} of N-4 sample also shifts redward with the increase of the system pressure. When the pressure is increased to 6.2 GPa, the Raman peak splits, and the system undergoes a phase transition. When the pressure reaches 16.7 GPa, the characteristic peak shifts to 559 cm^{-1} without obvious broadening. When the system is depressurized, the characteristic peak also shifts blueward and gradually returns to its original state, proving that the phase transition of N-4 under high pressure is also a reversible phase transition. According to the fitting results in Fig. 8d and e, the Raman shift of N-4 under different pressures is better fitted linearly. After the phase transition, the shift of the characteristic peak still shows a linear relationship with the change of pressure, and the shift change is obvious, approximately 5.87 cm^{-1}/Gpa. It can be seen that perovskite materials have application prospects in pressure sensing.

4. Conclusions

In this paper, $Na_8Al_6Si_6O_{24}Cl_2$ was synthesized by the high-temperature solid-phase method under different atmospheres. The luminescence characteristics of $Na_8Al_6Si_6O_{24}Cl_2$ were investigated and its luminescence mechanism model was constructed. Combining diamond pressure chamber and laser Raman spectroscopy technology, $Na_8Al_6Si_6O_{24}Cl_2$ synthesized under the conditions of 8 % H_2 + 92 %N_2 and Ar atmosphere was selected for high-pressure experiments. The results show that the luminescence band of $Na_8Al_6Si_6O_{24}Cl_2$ can be regulated. The fluorescence emitted by the samples synthesized under 8 %H_2 and 92 %N_2 is closer to blue light, while the samples synthesized under air conditions, double crucible method conditions and Ar gas atmosphere all significantly shift towards green light. The luminescence of $Na_8Al_6Si_6O_{24}Cl_2$ under the condition of 8 % H_2 and 92 %N_2 can be attributed to V_O, while the luminescence under the Ar gas atmosphere can be attributed to Vo-V_{Al}. The $Na_8Al_6Si_6O_{24}Cl_2$ synthesized under the Ar atmosphere has excellent performance in pressure sensing, and the Raman shift change under high pressure can reach 5.87 cm^{-1}/Gpa. The dual functions of this material have broad application prospects in the construction of "light-pressure" dual-modal intelligent sensing systems.

CRediT authorship contribution statement

Chuchu Song: Writing – original draft, Formal analysis, Data curation. **Yafang Wang:** Investigation. **Qingfeng Guo:** Writing – review & editing. **Libing Liao:** Writing – review & editing. **Changqing Jin:** Software. **Zheng Deng:** Investigation, Data curation.

Declaration of Competing Interest

We declare that we have no financial and personal relationships with other people or organizations that can inappropriately influence our work, there is no professional or other personal interest of any nature or kind in any product, service and/or company that could be construed as influencing the position presented in, or the review of, the manuscript entitled, "Study on the luminescence mechanism and pressure sensing properties of undoped $Na_8Al_6Si_6O_{24}Cl_2$".

Acknowledgment

This study was supported by the National Science and Technology Infrastructure-The National Infrastructure of Mineral, Rock and Fossil Resources for Science and Technology (http//www.nimrf.net.cn, accessed on 25 December 2021), as well as the Program of the Data Integration and Standardization in the Geological Science and Technology from MOST, China, grant number 2013FY110900–3. Chuchu Song would like to thank the College Student Research Innovation Program of China University of Geosciences, Beijing and the Innovation and Entrepreneurship Training Program of China University of Geosciences, Beijing.

Appendix A. Supporting information

Supplementary data associated with this article can be found in the online version at doi:10.1016/j.jallcom.2025.182172.

References

1 H.A. Klasens, A.H. Hoekstra, A.P.M. Cox, Ultraviolet fluorescence of some ternary silicates activated with lead, J. Electrochem. Soc. 104 (2) (1957) 93–100.
2 P.B. Moore, T. Araki, Atomic arrangement of merwinite, $Ca_3Mg[SiO_4]_2$, an unusual dense-packed structure of geophysical interest, Am. Miner. 57 (1972) 1355–1374.
3 X. Zhu, X. Tong, Z. Li, et al., Atomically embedded synergetic dual-metal catalysis FeO&MoS_2 nanoparticles on sodalite structural zeolite toward electrochemical methanol oxidation reaction, Chem. Eng. J. 471 (2023) 144632.
4 E.M. Pierce, K. Lilova, et al., Structure and thermochemistry of perrhenate sodalite and mixed guest perrhenate/pertechnetate sodalite, Environ. Sci. Technol. 51 (2) (2017) 997–1006.
5 J.A. Armstrong, M.T. Weller, Structural observation of photochromism, Chem. Commun. (10) (2006) 1094–1096.
6 M. Yu, D. Luo, J. Kuang, W. Yuan, Synthesis and luminescence properties of Eu^{3+} doped sodalite phosphors using Kaolin, Results Phys. 41 (2022) 105887.
7 D.E.W. Vaughan, H.P. Yennawar, A.J. Perrotta, Synthesis and structure of large optically clear crystals of gallogermanate sodalite, Cryst. Growth Des. 6 (9) (2006) 2072–2075.
8 S.W. Wi, Y.S. Lee, Effect of Eu^{3+}, Bi^{3+}, and Li^{+} doping on luminescent property of $GdNbO_4$, J. Rare Earths 42 (1) (2022) 66–75.
9 M. Kaiheriman, A. Maimaitinaisier, A. Rehiman, A. Sidike, Photoluminescence properties of green and red luminescence from natural and heat-treated sodalite, Phys. Chem. Min. 41 (3) (2014) 227–235.
10 J. Yang, Y. Su, H. Li, X. Liu, Z. Chen, Hydrothermal synthesis and photoluminescence of Ce^{3+} and Tb^{3+} doped $La_2Sn_2O_7$ nanocrystals, J. Alloy. Compd. 509 (31) (2011) 8008–8012.
11 H. Zhu, E. Zhu, H. Yang, L. Wang, D. Jin, K. Yao, High-brightness $LaPO_4$:Ce^{3+}, Tb^{3+} nanophosphors: reductive hydrothermal synthesis and photoluminescent properties, J. Am. Ceram. Soc. 91 (5) (2008) 1682–1685.
12 I. Norrbo, J.M. Carvalho, P. Laukkanen, et al., Lanthanide and heavy metal free long white persistent luminescence from Ti doped Li-hackmanite: a versatile, low-cost material, Adv. Funct. Mater. 27 (17) (2017) 1606547.
13 I. Norrbo, P. Gluchowski, I. Hyppänen, et al., Mechanisms of tenebrescence and persistent luminescence in synthetic hackmanite $Na_8Al_6Si_6O_{24}(Cl,S)_2$, ACS Appl. Mater. Interfaces 8 (18) (2016) 11592–11602.
14 C. Agamah, S. Vuori, P. Colinet, et al., Hackmanite—the natural glow-in-the-dark material, Chem. Mater. 32 (20) (2020) 8895–8905.
15 N.V. Chukanov, S.M. Aksenov, Structural features, chemical diversity, and physical properties of microporous sodalite-type materials: a review, Int. J. Mol. Sci. 25 (18) (2024) 10218.
16 F. Blumentritt, M. Vigier, E. Fritsch, Blue persistent luminescence (phosphorescence) of sodalite, J. Gemmol. 37 (6) (2021) 1–4.
17 C.Z. Van Doorn, D.J. Schipper, Luminescence of O_2^-, Mn^{2+} and Fe^{3+} in sodalite, Phys. Lett. A 34 (3) (1971) 139–140.
18 I.F. Chang, A. Onton, Optical properties of photochromatic sulfur-doped chlorosodalite, J. Electron. Mater. 2 (1) (1973) 17–46.
19 S. Park, T. Vogt, Defect monitoring and substitutions in $Sr_{3-x}A_xAlO_4F$ (A = Ca, Ba) oxyfluoride host lattices and phosphors, J. Phys. Chem. C 114 (26) (2010) 11576–11583.
20 K. Oskam, K. Kaspers, A. Meijerink, H. Müller-Bunz, T. Schleid, Luminescence of $La_3F_3(Si_3O_9)$:Ce^{3+}, J. Lumin 99 (2) (2002) 101–105.
21 C. Zhang, C. Lin, C. Li, Z. Quan, X. Liu, J. Lin, Enhanced luminescence of BPO_4 by mixing with SiO_2 and Al_2O_3, J. Phys. Chem. C. 112 (6) (2008) 2183–2192.
22 W.L. Medlin, Trapping centers in thermoluminescent calcite, Phys. Rev. 135 (1964) A1770–A1779.
23 Y. Han, Q. Mo, Z. Ma, et al., Stable long-persistent luminescence from self-activated $CaSb_2O_6$ induced by intrinsic defects, Nano Lett. 24 (45) (2024) 14453–14459.

24 S.S. Melo, T.S. Lilge, M.A. Gomes, et al., Undoped $CdSiO_3$ for contactless thermometer in the cryogenic range: pH-dependent intrinsic defects and emitting colour, J. Solid State Chem. 321 (2023) 123908.
25 G.S. Polymeris, G. Kitis, N.C. Tsirliganis, Correlation between TL and OSL properties of CaF_2, N. Nucl. Instrum. Methods Phys. Res. Sect. B 251 (2006) 133–142.
26 H. Gobrecht, D. Hofmann, Spectroscopy of traps by fractional glow technique, J. Phys. Chem. Solids 27 (1966) 509–522.
27 C. Song, Q. Guo, Y. Wang, L. Liao, Thermoluminescence characteristics of UV-irradiated natural hackmanite, Thermochim. Acta 742 (2024) 179879.
28 K. Siemek, A. Olejniczak, L.N. Korotkov, et al., Investigation of surface defects in $BaTiO_3$ nanopowders studied by XPS and positron annihilation lifetime spectroscopy, Appl. Surf. Sci. 578 (2022) 151807.
29 R.V.K. Mangalam, A. Chakrabarti, et al., Identifying defects in multiferroic nanocrystalline $BaTiO_3$ by positron annihilation techniques, J. Phys. Condens. Matter 21 (44) (2009) 445902.
30 D. Wang, et al., Positron annihilation study of the interfacial defects in ZnO nanocrystals: correlation with ferromagnetism, J. Appl. Phys. 107 (2) (2010) 023524.
31 H. Luitel, S. Sarkar, et al., Positron annihilation lifetime characterization of oxygen ion irradiated rutile TiO_2, Nucl. Instrum. Methods Phys. Res. Sect. B 379 (2016) 215–218.
32 M.J. Puska, R.M. Nieminen, Theory of positrons in solids and on solid surfaces, Rev. Mod. Phys. 66 (3) (1994) 841.
33 B. Barbiellini, M.J. Puska, T. Torsti, et al., Gradient correction for positron states in solids, Phys. Rev. B 51 (11) (1995) 7341.
34 R.M. Nieminen, E. Boronski, L.J. Lantto, Two-component density-functional theory: application to positron states, Phys. Rev. B 32 (2) (1985) 1377.
35 Q. Yang, X. Cao, B. Wang, et al., Systematic investigation of positron annihilation in transition metals from first principles, Phys. Rev. B 108 (10) (2023) 104113.
36 Y. Huang, W. Fan, Y. Hou, K. Guo, Y. Ouyang, Z. Liu, Effects of intrinsic defects on the electronic structure and magnetic properties of $CoFe_2O_4$: a first-principles study, J. Magn. Magn. Mater. 429 (2017) 263–269.
37 L. Ning, X. Cheng, et al., Energetic, optical, and electronic properties of intrinsic electron-trapping defects in $YAlO_3$: a hybrid DFT study, J. Phys. Chem. C 118 (34) (2014) 19940–19947.
38 N.B. Bolotina, A.N. Sapozhnikov, N.V. Chukanov, M.F. Vigasina, Structure modulations and symmetry of lazurite-related sodalite-group minerals, Crystals 13 (2023) 768.
39 J. Ariai, S.R.P. Smith, The Raman spectrum and analysis of phonon modes in sodalite, J. Phys. C Solid State Phys. 14 (8) (1981) 1193.
40 M.K. Badrinarayan, J.M. Stencel, L.T., Jr Todd, Raman scattering study of the coloration mechanism of cathodochromic sodalite, J. Phys. Chem. 84 (4) (1980) 456–459.